

# Symmetry Breaking in Chemical Systems: Engineering Complexity through Self-Organization and Marangoni Flows

Sangram Gore<sup>1†</sup>, Binaya Paudyal<sup>1†</sup>, Mohamed Ali<sup>1</sup>, Nader Masmoudi<sup>1,2</sup>,  
Albert Bae<sup>3</sup>, Oliver Steinbock<sup>4</sup>, Azam Gholami<sup>1\*</sup>

<sup>1</sup>Science Division, New York University Abu Dhabi, Abu Dhabi, UAE

<sup>2</sup>Courant Institute of Mathematical Sciences, New York University, New York, USA

<sup>3</sup>Lewis & Clark College, Portland, Oregon, USA.

<sup>4</sup>Department of Chemistry and Biochemistry, Florida State University  
Tallahassee, Florida, USA

<sup>†</sup> These authors contributed equally to this work.

\* Corresponding author: [azam.gholami@nyu.edu](mailto:azam.gholami@nyu.edu).

**In this study, we investigate the impact of a periodic array of hydrophilic cylindrical obstacles on the spatio-temporal dynamics of chemical waves in the bubble-free Belousov-Zhabotinsky-1,4-cyclohexanedione (BZ-CHD) oscillatory chemical reaction. We find that the thin fluid layer ascending the outer surfaces of these hydrophilic obstacles is crucial for influencing wave dynamics. We observe that circular waves begin almost simultaneously at these obstacles and spread outward. In a covered setup where evaporation is minimal, these wavefronts retain their circular shape. However, in an open setup where evaporative cooling is more pronounced, thermal Marangoni flows trigger wavefront instabilities, leading to the formation of distinctive flower-like patterns around the obstacles. Our experiments also shows that the number of petals formed increases linearly with the diameter of the pillars, though a**

**minimum diameter is required for the instabilities to manifest. These results highlight the ability to 'engineer' specific wave patterns, offering a strategy to control and steer the reaction dynamics. This capability is particularly crucial for the development of microfluidic devices that demand precise control over chemical wave propagation.**

## **Introduction**

The Belousov-Zhabotinsky (BZ) reaction is a prime example of a non-equilibrium chemical oscillator, renowned for its spontaneous generation of complex wave patterns such as spirals and target waves [1–4]. The introduction of obstacles within the BZ-CHD variant of this reaction [5–12] can profoundly influence both pattern formation and wave propagation within the reactive media. These obstacles serve to either disrupt the existing symmetry, stabilizing or destabilizing emergent patterns, thereby orchestrating the creation of intricate spiral waves or inducing localized turbulence based on their spatial arrangement and the physical characteristics of the medium. These obstacles can serve as more than mere physical interruptions; they can interact dynamically with the chemical processes at play and modify the local environment of the reaction by altering the flow and diffusion of reactants, which in turn affects the kinetics of the reaction. Obstacles might create regions of concentrated reactants or products due to differential flow patterns around their surfaces, leading to variations in reaction speed and wave propagation characteristics. Gaining an understanding of these interactions offers valuable insights into mastering pattern control in both chemical and biological systems [13], paving the way for advanced manipulation and utilization of these complex behaviors.

Marangoni flows have a profound impact on the dynamics and patterns that emerge in the BZ reaction [14–25]. These flows are initiated by gradients in surface tension [23, 26], which might arise from either temperature variations (thermocapillary effect) or differences in so-

lute concentrations (solutocapillary effect) across the fluid's surface. These gradients cause the fluid to migrate from regions of lower to higher surface tension, amplifying effects such as fluid climbing, often initiated by capillary action. In an open setup, where evaporative cooling induces thermal Marangoni instabilities, the interplay of chemical waves, buoyancy-driven flows due to density gradients, and surface-driven flows resulting from surface tension gradients collectively influences pattern formation [19, 20, 27–32]. The introduction of obstacles can further enhance these dynamics, leading to instabilities like fingering. How the fluid interacts with these obstacles varies depending on their surface properties, such as whether they are hydrophilic or hydrophobic. Hydrophilic surfaces, for instance, tend to augment fluid climbing through a combination of capillary action and Marangoni flows.

While Marangoni flows tend to propel the fluid upward or along surfaces, gravity serves as a counteracting force, pulling the fluid downward. This ongoing tug of war can generate undulations or waves at the fluid interface, potentially developing into finger-like patterns if the fluid becomes sufficiently unstable [33–36]. Generally, gravity acts to stabilize the fluid layer by promoting a more uniform, flat configuration, whereas Marangoni effects can destabilize it, leading to uneven distributions of fluid. In instances where Marangoni flows excessively thin the fluid layer in certain areas, these regions become susceptible to the formation of droplets or fingers, influenced by gravitational pull or other external disturbances. This intricate balance between Marangoni flows and gravity critically influences the complex patterns and behaviors seen in such reactive fluid systems.

In this work, we demonstrate that in the BZ-CHD reaction, a periodic arrangement of hydrophilic cylindrical obstacles acts as central points for emitting synchronously circular waves. Additionally, in an open setup where evaporation cooling is significant, thermal Marangoni flows trigger a fingering instability, leading to the prominent formation of distinct flower-like wave patterns. Notably, the number of petals formed increases with the increasing perimeter of

the pillars. We conducted numerical simulations of a reaction-diffusion model [37] to understand wave dynamics observed in the experiments.

## Results

### Experimental Results

Our quasi 2D setup consists of a periodic array of millimeter-sized PDMS-based cylindrical obstacles (see Fig. 1A and Materials and Methods) that influence the spatio-temporal dynamics of chemical waves. The PDMS has undergone plasma treatment to make it hydrophilic, which allows the fluid to climb up around these obstacles, as illustrated in Fig. 1B. We observe circular oxidation waves that initiate almost synchronously at the pillars, spreading outward at a speed of approximately 7 mm/min and recurring every minute (see Fig. 1). When these waves meet, they mutually annihilate, demonstrating the typical behavior of an excitable medium. The time evolution of these waves is significantly affected by whether the setup is open or covered, which alters the evaporation rate of the liquid. We discuss the outcomes for both the covered and open setups below.

#### **Covered setup: Circular waves initiate synchronously at the pillars and maintain their circular shape**

In a covered setup, chemical waves begin nearly simultaneously on the pillars, with a wave period of about one minute, and maintain their circular shape across multiple wave cycles (Fig. 1C-D and Video 1). A space-time plot along an arbitrary line crossing the obstacles illustrates that they serve as wave centers (Fig. 1G). Additionally, to visualize the wave dynamics over several cycles, we compiled the light intensity data along an arbitrary circle surrounding a pillar, confirming that the wavefronts consistently retain their circular form (Fig. 1H). Figure 1K presents a separate experiment where the entire Petri dish is imaged, demonstrating similar wave dy-

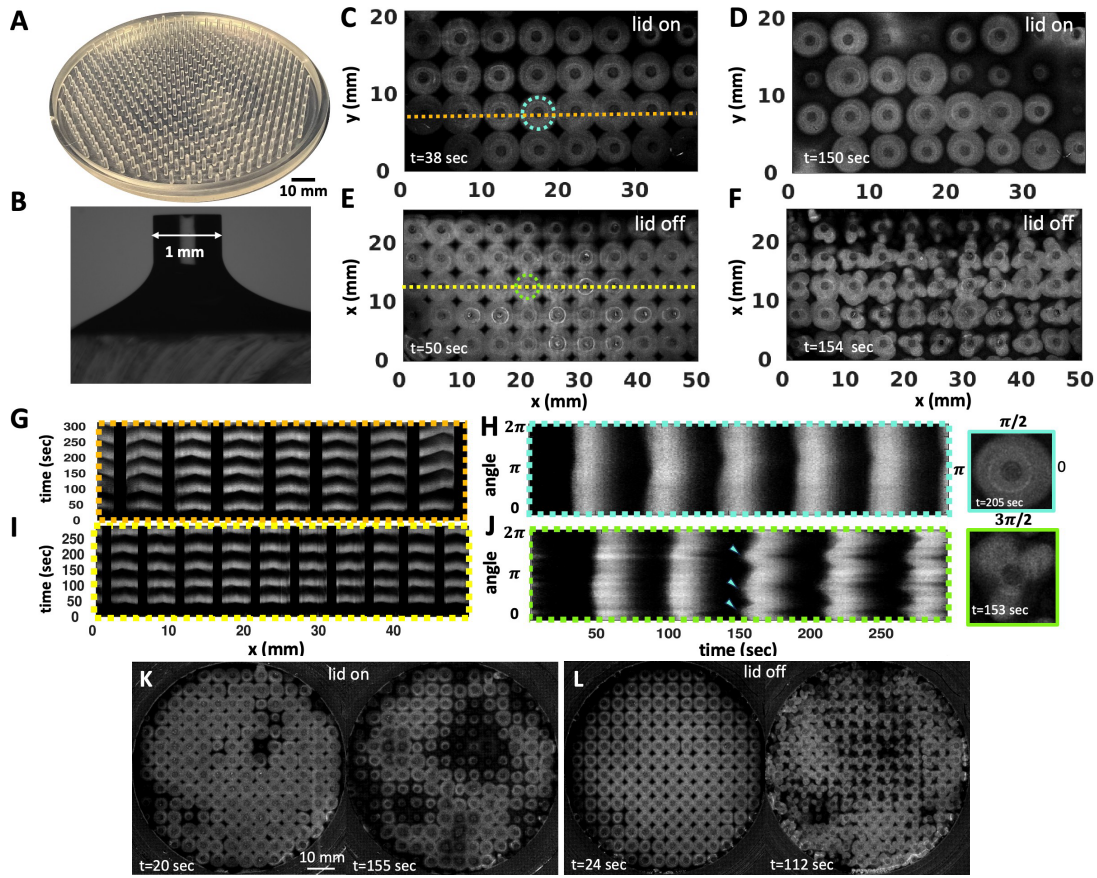


**Figure 1: Wave dynamics in a covered versus an open setup.** (A) A standard experimental setup featuring a periodic arrangement of PDMS-based cylindrical obstacles designed to fit within a 10 mm Petri dish. (B) A side view depicting the fluid profile around an exemplary hydrophilic pillar. (C-D) Top views of concentric chemical waves in a covered setup, captured at two distinct times, show the waves initiating almost simultaneously at the pillars and spreading outward. The waves retain their circular shapes over time. (E-F) Top views of chemical waves captured at two distinct times in an open setup: initially, concentric waves form around the obstacles (E), and later, the wave fronts fracture to create flower-like patterns (F). (G) A space-time plot along the orange line indicated in (C) demonstrates that the pillars serve as the wave centers. Black bars show the position of the obstacles. (H) A space-time plot traced along the cyan-colored circle shown in (C) illustrates that the circular waves retain their shape through multiple wave cycles. (I) The space-time plot along the yellow line shown in (E). (J) The space-time diagram along the green circle indicated in (E) illustrates that after two cycles of circular waves, the wave fronts break. In this experiment, where pillars are 1 mm in diameter, 3 mm tall, and spaced 5 mm apart, most pillars develop three petals. (K-L) Images showing the entire Petri dish in two separate experiments. The timestamps reflect the elapsed time since the start of recording, which began shortly after the chemical solution was introduced into the PDMS-made setup. These images are typical of at least 50 experiments.

namics (Video 2).

**Open setup: Circular waves begin synchronously at the pillars and eventually evolve into flower-like patterns**

In an open setup, where evaporation is more significant, the obstacles continue to act as centers that emit synchronous concentric waves (Fig. 1E, I and Video 3). However, after approximately two cycles of these circular waves, an instability in the wavefront becomes apparent: the circular wave fronts fragment, leading to the formation of striking flower-like patterns (see Fig. 1F, J). Figure 1L presents a separate experiment where the entire Petri dish is imaged, demonstrating similar wavefront instability (Video 4).

Our experimental findings indicate that the number of petals is influenced by the diameter of the pillars. Typically, pillars with a diameter of 1 mm form three petals (Fig. 1F), while those with a diameter of 1.5 mm often produce four petals, and pillars measuring 3.8 mm in diameter generate seven to eight petals (Figs. 2 and 5). Figure 2 presents an illustrative experiment where the pillar diameters alternate between 1 mm and 1.5 mm across neighboring rows, with the top row featuring pillars of 1.5 mm in diameter. In this setup, the 1 mm pillars typically form patterns with three petals, whereas the 1.5 mm pillars display flower patterns consisting of four petals (see Fig. 2B-E and Video 5). Interestingly, we noted that the number of petals can change over time, as illustrated in Fig. 2F. In a related observation, Fig. 3 depicts an experiment where, after two cycles of circular wavefronts, the wavefronts around the pillar break. Initially, four petals form, but as time progresses, a fifth petal develops (Fig. 3C). The synchronization between the waves initiated at different pillars is demonstrated through a phase map calculated using the Hilbert transform (see Materials and Methods), as shown in Figs. 3A-B. In this experiment, where we have captured images of the entire small Petri dish, the waves initiated at the PDMS boundary also exhibit wavefront instability, similar to those observed at the pillars (see Fig. 3D and Video 6).

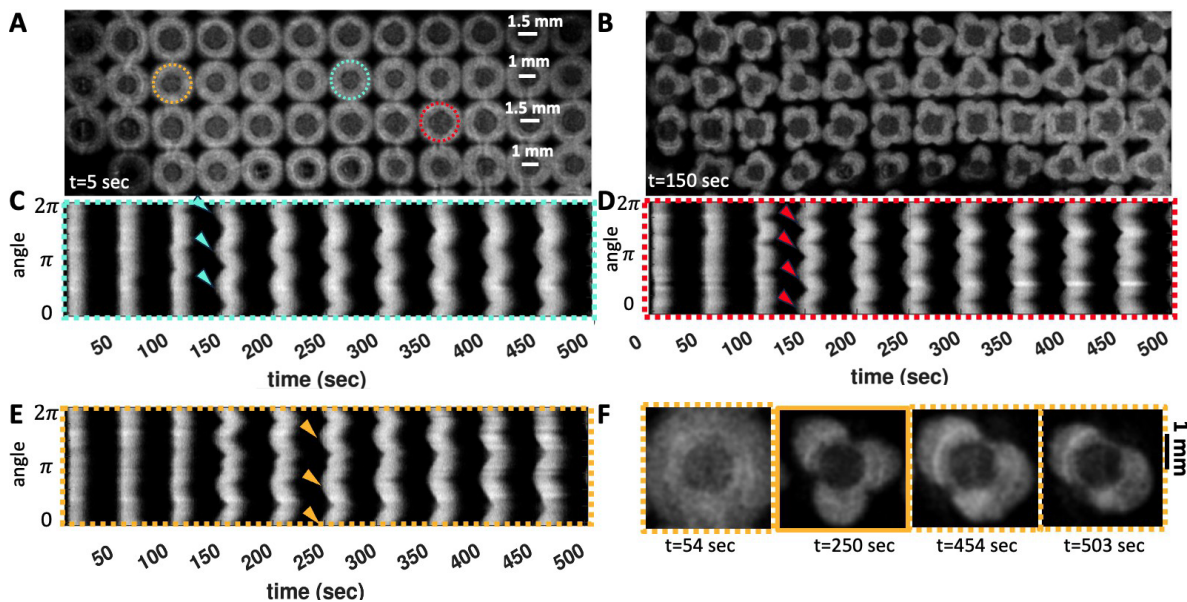


**Figure 2: Number of petals depends on the pillar diameter and can vary over time.** (A-B) Top views of chemical waves captured before and after the onset of instability in an experiment where pillar diameters alternate between rows, with 1.5mm pillars in the top row and 1mm pillars in the second row. Pillars with a diameter of 1.5mm generally develop four petals, whereas those with a diameter of 1mm typically produce three petals. (C-E) Space-time plots along the highlighted circles in panel (A) illustrate the progression of the instability. (F) An example of a pillar that initially developed three petals, but over time, two of the petals merged.

To unravel the mechanisms (i) governing the formation of synchronous circular waves around the pillars and (ii) contributing to the instability of the wavefront in an open setup, we began by examining the hypothesis that the permeability of PDMS to bromine gas (and potentially other chemicals) facilitates wave formation on the pillars, an idea supported by literature [38]. To test this possibility, we conducted experiments using PDMS pillars coated with a thin layer of gold (approximately 200 nm thick, see Fig. S1E). Contrary to expectations, the pillars continued to function as centers for synchronous wave activity even with the gold coating, which blocks chemical absorption. Additionally, we conducted experiments using obstacles made of acrylic with plasma treatment and observed that these pillars also functioned as

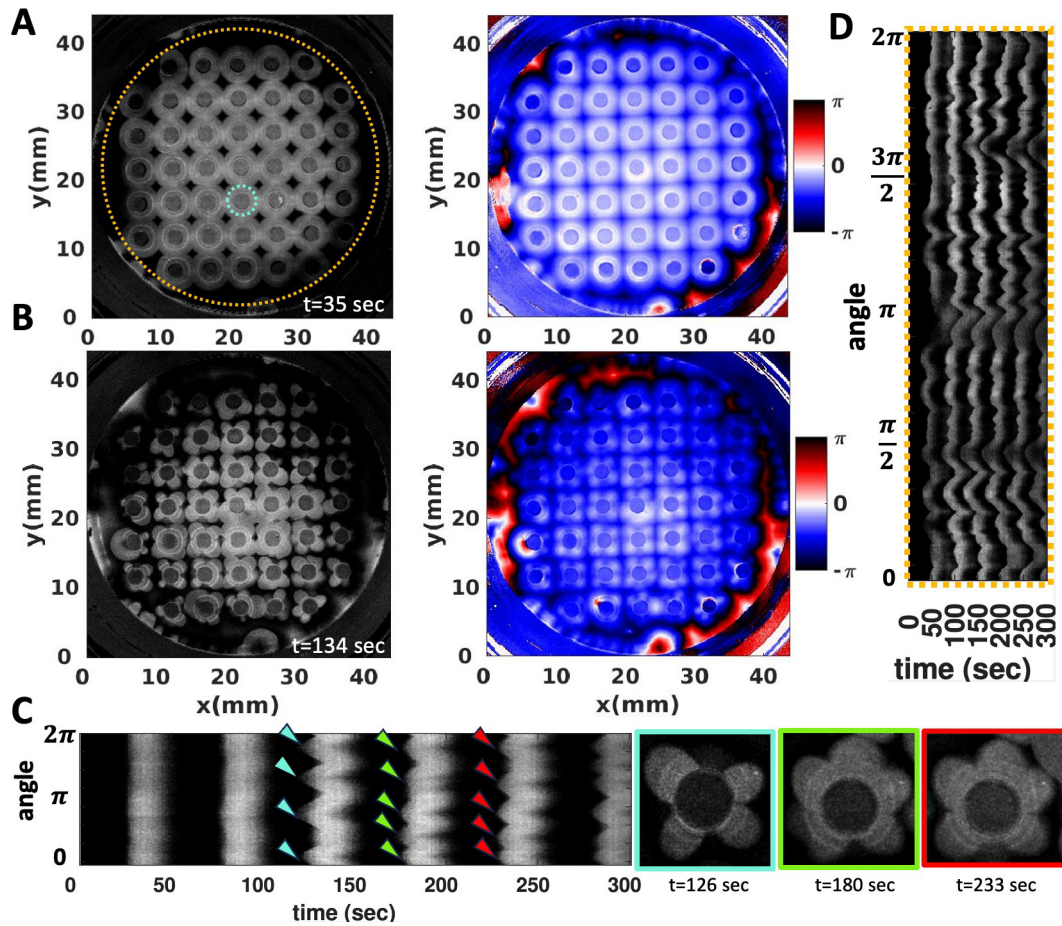


Figure 3: **Wavefront instability at the periphery.** (A-B) Pillars with a diameter of 1.85mm typically form four petals. (C) A space-time plot along the cyan-highlighted circle in panel A shows the development of the instability, with a noticeable evolution in the number of petals over time. (D) A space-time plot along the orange-highlighted circle demonstrates the wavefront instability that also manifests at the PDMS wall on the periphery. This experiment is conducted in a small open Petri dish.

centers for wave activity (see Video 7). These results confirm that the absorption of chemicals into PDMS is not the primary mechanism driving the formation of concentric waves around the obstacles.

Next, we explored the impact of the thin liquid layer ascending the PDMS-made pillars, which are hydrophilic due to plasma treatment. Our investigation involved several experimental

approaches. Initially, we conducted experiments with pillars that had not undergone plasma treatment and observed that most of the pillars did not act as centers for wave generation (see Fig. S7 and Video 8). Subsequently, we decreased the height of the pillars from 3 mm to 1 mm, ensuring that these shorter pillars were submerged to the same fluid level. We noted that the submerged pillars also did not act as wave centers (see Video 9). Lastly, to determine if the generation of circular waves around the pillars was influenced by the proximity of adjacent pillars, we conducted tests with a solitary pillar. As depicted in Fig. S4 and Video 10, this isolated pillar also became a center for wave activity and further demonstrated wavefront instability in an open setup. These experiments collectively affirm that the climbing liquid layer on the pillars is crucial in the generation of synchronous circular waves.

### **Experimental evidence of a fingering instability**

As described earlier, our experiments reveal that the climbing film on the external surfaces of cylindrical pillars significantly influences the formation of synchronous circular waves and wavefront instability. We observe that wavefront instability occurs primarily in open experimental setups where evaporation is more pronounced than in covered setups. It is reasonable to suggest that the thin, ascending liquid layer evaporates quicker than the thicker parts, creating a minor temperature gradient. This gradient induces a surface tension gradient, which in turn generates Marangoni flows. The observation that waves originate from the thin ascending fluid layer aligns with findings from another experiment in which we slightly tilted the Petri dish [16]. In this setup, we noted that synchronization waves first emerged in areas with lower fluid thickness (see Fig. S5 and Video 11). Literature reveals that Marangoni-driven thin films on planar or curved substrates exhibit a complex array of dynamics [33,36,39], dependent on the flat upstream film thickness trailing the advancing front. The thickness of this film is influenced by the meniscus curvature at the fluid source (see Fig. 1B) and the interplay of the thermally-

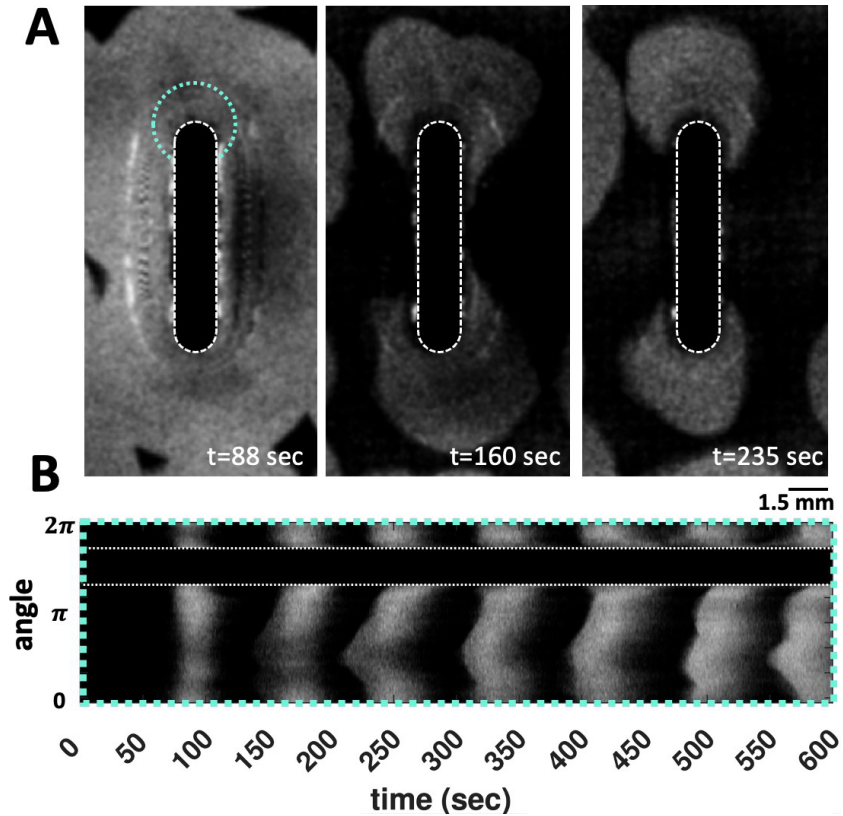


Figure 4: **Experiment with rounded rectangular obstacle geometry.** (A) In an experiment examining the impact of evaporation, obstacles with a rectangular body and rounded ends were used. The sequence of wave pattern images indicates that instability mainly arises at the curved ends. (B) A space-time plot along the circular path marked in panel A illustrates the progression of wavefront instability. These images are representative of at least 20 experiments.

induced surface tension gradient with gravity. It is also important to note that surface tension gradients, which lead to Marangoni flows, may also arise from chemical concentration gradients (see Fig. S2). The interplay between Marangoni flows and gravity can disrupt the contact lines, evolving into a finger pattern. Specifically, the linear stability analysis in Ref. [36] correlates the number of fingers with the cylindrical pillar's perimeter, aligning with our findings (see Fig. 2 and Fig. 5). This analysis also suggests a minimum pillar diameter threshold below which fingering instability does not occur. To validate this, we reduced the pillar diameter to 0.5

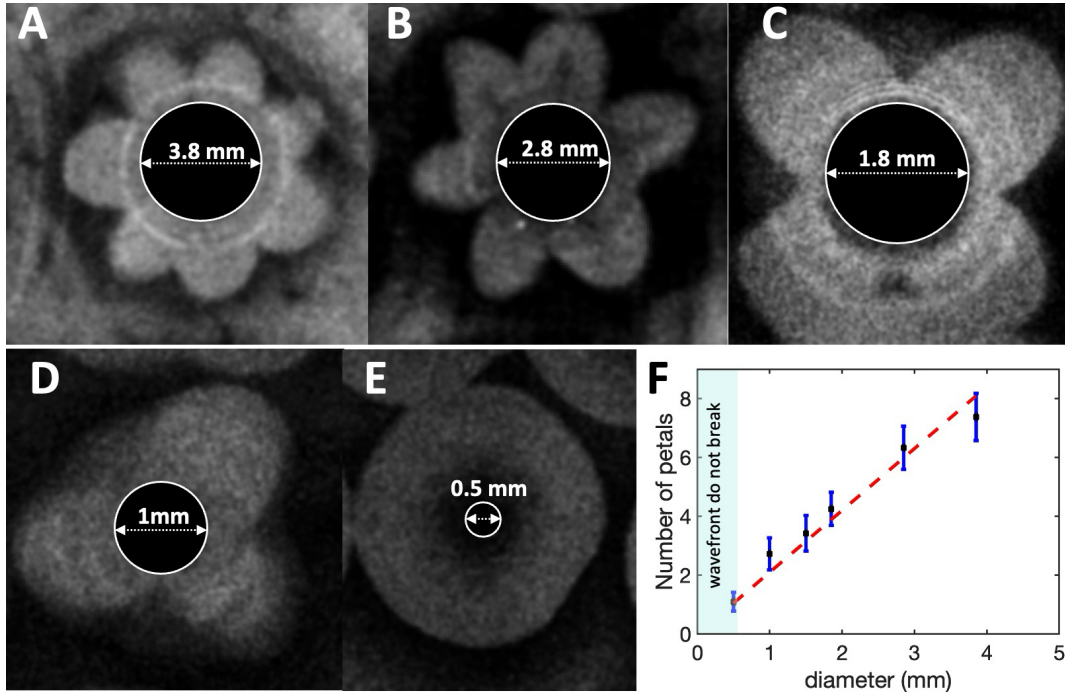


Figure 5: **Effect of the pillar diameter on the number of petals.** **A-D)** As the pillar diameter decreases, so does the number of petals formed. For instance, pillars with a diameter of 3.8 mm typically develop around 7 petals, while those with a diameter of 2.8 mm produce about 6 petals. This number drops to 4 petals for pillars with a diameter of 1.8 mm, and further reduces to 3 petals for those with a diameter of 1 mm. **E)** Pillars with a diameter of 0.5 mm exhibit no wave front instability, which verifies that there is a minimum pillar perimeter required for such instability to develop. **F)** The number of petals increases linearly with the diameter of the pillar. Below a critical diameter, wavefronts do not break and remain circular.

mm in our open setup experiments, observing that the wavefronts remained nearly circular (see Fig. S3). Additionally, we tested the impact of evaporation on fingering instability using obstacles with a rectangular geometry and circular ends (see Fig. 4). Given the increased surface area at the curved boundaries, we anticipated a higher evaporation rate here, which likely triggers the fingering instability predominantly at these locations, a hypothesis supported by our observations. Finally, we conducted a control experiment using an open, plasma-treated glass Petri dish without any obstacles (refer to Fig. S8). Interestingly, we observed wavefront instability

at the glass boundary, which closely resembled the phenomena observed at the PDMS wall in Fig.3. This experiment confirms that the thin layer of climbing fluid at the boundary is critical for initiating waves, and that evaporation significantly contributes to the wavefront instability.

## Numerical Simulations

We conducted numerical simulations using the Tyson-Fife model [37] to understand wave dynamics observed in the experiments (refer to Materials and Methods for details). In our simulations, we applied a boundary condition based on the hypothesis that the inhibitor  $w$  (bromide ions) is depleted at the pillars due to evaporation. This assumption is supported by experimental observations where the fluid ascends the hydrophilic pillars, forming a thin film subject to more rapid evaporation compared to the bulk solution. Simulation results, as displayed in Fig. 6, set the inhibitor  $w$  to zero at the locations of the pillars. The depletion of bromide ions near the obstacles results in an increased concentration of bromate available to oxidize the metal catalyst, thus initiating oxidation waves at the obstacles. This is in agreement with our experimental observations.

Next, we investigated how fingering patterns affect wave dynamics by analyzing the impact of an uneven angular distribution of  $w$  around the obstacles (refer to Materials and Methods for more information). The results of this analysis are presented in Fig. 6C and Fig. S6. Depending on the asymmetry introduced, a varying number of petals emerge following at least one initial cycle of circular waves. Remarkably, even with a set asymmetry of  $w$  near the obstacles, the orientation and size of the petals can vary as the simulation progresses.

## Discussion

In this study, we introduce a periodic array of hydrophilic obstacles into the BZ-CHD reaction which quickly turn them into synchronous centers of wave activity. The thin layer of chemical

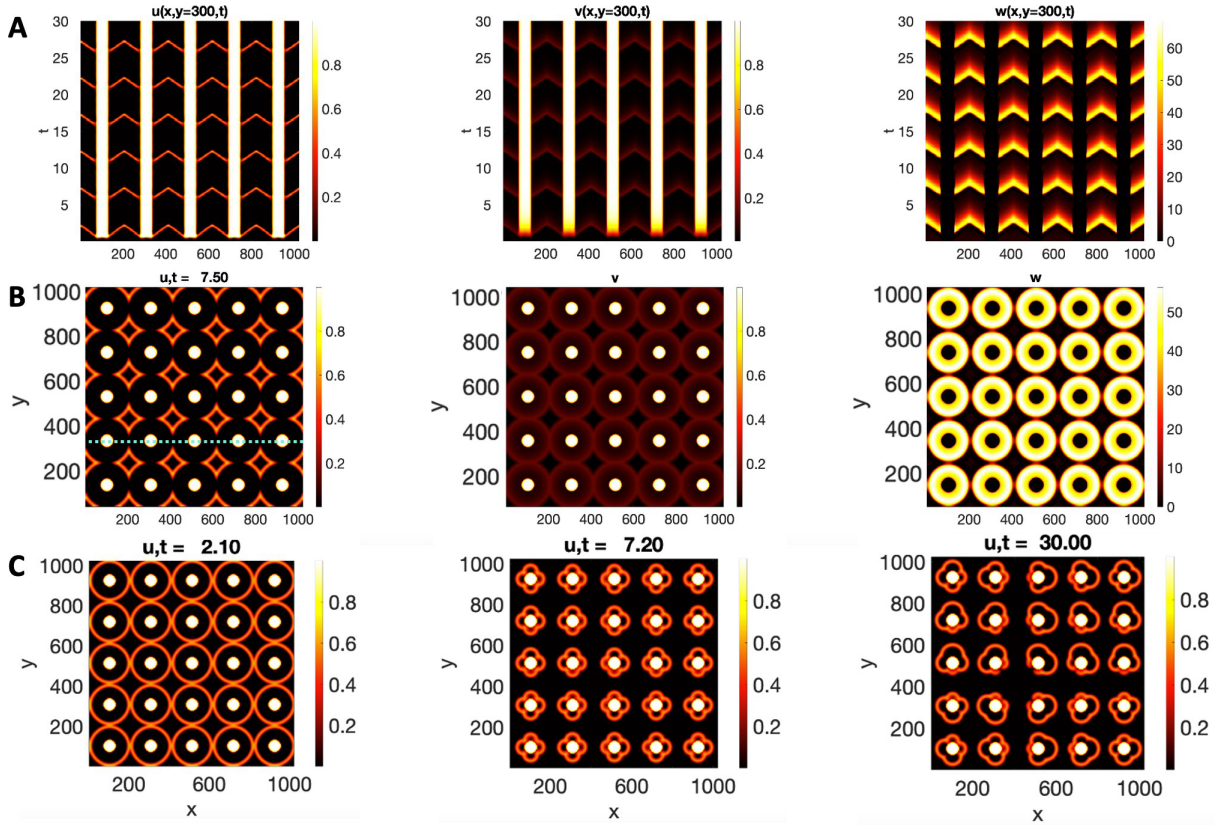


Figure 6: **Numerical simulations of the Tyson-Fife model with periodic array of obstacles.** (A) The space-time plot along the line marked in panel B illustrates that the obstacles become wave centers. (B) shows an image of the circular waves emanating from the obstacles at dimensionless time  $t = 7.5$ . Time and space are in arbitrary units. (C) Simulations incorporating an asymmetric distribution of the inhibitor  $w$  around the obstacles demonstrate wavefront instability at different time points. Only concentration of activator  $u$  is shown; see Fig. S6 for space-time plots and concentrations of  $v$  and  $w$ .

solution that ascends the outer surface of the obstacles plays a crucial role in enabling them to function as wave centers, effectively determining the spatial positioning of these centers (Fig. 1). While a single isolated obstacle can also serve as a wave center (Fig. S4), the presence of an obstacle array helps to prevent the formation of other random wave centers. In a covered setup where evaporation is minimal, wavefronts maintain their circular shapes through multiple wave cycles. Conversely, in an open setup where evaporation plays a substantial role, Marangoni-

driven fingering instability occurs and wavefronts break, leading to the formation of striking flower-like wave patterns (Fig. 1). The number of petals formed is linearly proportional to the diameter of the obstacles (Fig. 5), and a minimum diameter is necessary for this instability to occur (Fig. S3).

The behavior of a film climbing the exterior of a vertical cylinder, influenced by the opposing forces of a thermally driven surface tension gradient and gravity, is extensively explored in the literature through numerical analysis using a thin-film model (see review articles [40–42] and references therein). These models depend on three parameters: the cylinder radius, the upstream film height, and the downstream precursor film thickness. As the cylinder radius approaches infinity, the model converges to the scenario of a Marangoni-driven film ascending a vertical plate [33–35]. Ref. [36] investigates the stability of the contact line by introducing an infinitesimal two-dimensional perturbation to the traveling wave solution, characterized by sinusoidal variations in the azimuthal direction. Through linear stability analysis, the study determines that the traveling wave (the so called Lax shock) is unstable to long-wave perturbations at the contact line. Given the periodic nature of the contact line in the azimuthal direction, only an integer number of fingers can form along it. The analysis identifies the most unstable mode and a neutrally stable cutoff mode, beyond which all modes are stable. These modes increase linearly with the cylinder radius, indicating that the number of fingers formed along the contact line correlates with the cylinder’s circumference. There exists a critical cylinder radius below which the contact line remains stable, with no fingers forming. Our experimental results align with these theoretical findings. Future experiments that include sideways imaging of the pillars will be essential to directly visualize the fluid fingers in our experiments. Additionally, we aim to expand the numerical analysis from Ref. [36] to include the rounded rectangular obstacle geometry (Fig. 4), incorporating an asymmetric evaporation rate that results in an asymmetric surface tension gradient. Finally, we will couple the thin film equations of Ref. [36] with

the reaction-diffusion equations to capture the full dynamics of both the flow and the chemical components in the vicinity of the obstacles.

In our experiments, by tilting the Petri dish, it is possible to selectively control which array of obstacles initially becomes the focal point for wave generation (Fig. S5). As reported in Ref. [27] and consistent with our experiments, in an open tilted Petri dish, waves originate in the thinner areas of the fluid, where convective flows are negligible, and progress toward the thicker regions, where convective flows can develop due to evaporative cooling. They assumed that these convective flows generate a heterogeneous medium where the refractory tail of a preceding wave annihilates part of the following wavefront, resulting in segmented waves that curl inward to form spirals. Over time, a chaotic wave pattern develops. In another study to understand the role of the fluid thickness in an open Petri dish, Rossi et al. [19] have demonstrated that for fluid layers thinner than 1.0 mm, the BZ system behaves predominantly as a pure reaction-diffusion system, and convective effects are negligible. In layers with an intermediate thickness (1.0–3.0 mm), Marangoni instabilities dominate, allowing rippled waves to propagate without breaking, and segmented patterns are not observed. However, for layers thicker than 3.0 mm, buoyancy-driven flows become significant, and wave segmentation processes occur. Our experiment using an open, plasma-treated glass Petri dish with a fluid thickness of approximately 2 mm also revealed rippled wavefronts and Marangoni-driven mosaic patterns (Fig. S8A) [21–24]. We notice that at the boundary of the Petri dish, we observed a Marangoni-driven fingering instability, similar to the phenomena seen near the hydrophilic obstacles.

## References

- [1] I. R. Epstein, J. A. Pojman, *An introduction to nonlinear chemical dynamics: oscillations, waves, patterns, and chaos* (Oxford university press, 1998).

- [2] R. J. Field, R. M. Noyes, *The Journal of Chemical Physics* **60**, 1877 (1974).
- [3] A. Zaikin, A. Zhabotinsky, *Nature* **225**, 535 (1970).
- [4] J. J. Tyson, *The belousov-zhabotinskii reaction*, vol. 10 (Springer Science & Business Media, 2013).
- [5] T. Bánsági Jr, O. Steinbock, *Physical review letters* **97**, 198301 (2006).
- [6] C. T. Hamik, N. Manz, O. Steinbock, *The Journal of Physical Chemistry A* **105**, 6144 (2001).
- [7] N. Manz, B. T. Ginn, O. Steinbock, *The Journal of Physical Chemistry A* **107**, 11008 (2003).
- [8] C. T. Hamik, O. Steinbock, *New Journal of Physics* **5**, 58 (2003).
- [9] T. Bánsági, O. Steinbock, *Chaos: An Interdisciplinary Journal of Nonlinear Science* **18** (2008).
- [10] T. Bánsági Jr, O. Steinbock, *Physical Review E* **76**, 045202 (2007).
- [11] B. T. Ginn, O. Steinbock, *Physical review letters* **93**, 158301 (2004).
- [12] A. S. Mikhailov, K. Showalter, *Physics Reports* **425**, 79 (2006).
- [13] T. F. Eckstein, E. Vidal-Henriquez, A. J. Bae, A. Gholami, *Science signaling* **13**, eaaz3975 (2020).
- [14] S. Kai, H. Miike, *Physica A: Statistical Mechanics and its Applications* **204**, 346 (1994).
- [15] S. Kai, T. Ariyoshi, S. Inenaga, H. Miike, *Physica D: Nonlinear Phenomena* **84**, 269 (1995).

- [16] O. Inomoto, T. Ariyoshi, S. Inanaga, S. Kai, *Journal of the Physical Society of Japan* **64**, 3602 (1995).
- [17] I. R. Epstein, *et al.*, *Accounts of chemical research* **45**, 2160 (2012).
- [18] V. K. Vanag, I. R. Epstein, *Physical Chemistry Chemical Physics* **11**, 897 (2009).
- [19] F. Rossi, M. A. Budroni, N. Marchettini, J. Carballido-Landeira, *Chaos: An Interdisciplinary Journal of Nonlinear Science* **22** (2012).
- [20] F. Rossi, M. L. T. Liveri, *Ecological Modelling* **220**, 1857 (2009).
- [21] H. Miike, K. Miura, A. Nomura, T. Sakurai, *Physica D: Nonlinear Phenomena* **239**, 808 (2010).
- [22] K. Matthiessen, S. C. Müller, *Physical Review E* **52**, 492 (1995).
- [23] K. Matthiessen, H. Wilke, S. C. Müller, *Physical Review E* **53**, 6056 (1996).
- [24] M. A. Budroni, M. Masia, M. Rustici, N. Marchettini, V. Volpert, *The Journal of chemical physics* **130** (2009).
- [25] B. T. Ginn, B. Steinbock, M. Kahveci, O. Steinbock, *The Journal of Physical Chemistry A* **108**, 1325 (2004).
- [26] K. Yoshikawa, T. Kusumi, M. Ukitsu, S. Nakata, *Chemical physics letters* **211**, 211 (1993).
- [27] K. Agladze, V. Krinsky, A. Pertsov, *Nature* **308**, 834 (1984).
- [28] T. Plessner, H. Wilke, K. H. Winters, *Chemical physics letters* **200**, 158 (1992).
- [29] H. Wilke, *Physica D: Nonlinear Phenomena* **86**, 508 (1995).
- [30] L. Rongy, A. De Wit, *The Journal of chemical physics* **124** (2006).

- [31] H. Miike, S. C. Müller, B. Hess, *Chemical physics letters* **144**, 515 (1988).
- [32] D. Lohse, *Annual review of fluid mechanics* **54**, 349 (2022).
- [33] A. L. Bertozzi, A. Münch, X. Fanton, A. M. Cazabat, *Physical review letters* **81**, 5169 (1998).
- [34] A. L. Bertozzi, A. Münch, M. Shearer, *Physica D: Nonlinear Phenomena* **134**, 431 (1999).
- [35] A. Münch, A. Bertozzi, *Physics of Fluids* **11**, 2812 (1999).
- [36] L. B. Smolka, *Physical Review E* **96**, 043107 (2017).
- [37] J. J. Tyson, P. C. Fife, *The Journal of Chemical Physics* **73**, 2224 (1980).
- [38] P. R. Buskohl, R. A. Vaia, *Science advances* **2**, e1600813 (2016).
- [39] X. Fanton, A. Cazabat, D. Quéré, *Langmuir* **12**, 5875 (1996).
- [40] A. Oron, S. H. Davis, S. G. Bankoff, *Reviews of modern physics* **69**, 931 (1997).
- [41] D. Bonn, J. Eggers, J. Indekeu, J. Meunier, E. Rolley, *Reviews of modern physics* **81**, 739 (2009).
- [42] R. V. Craster, O. K. Matar, *Reviews of modern physics* **81**, 1131 (2009).

## Acknowledgments

We acknowledge fruitful discussions with professors G. Shubeita, A. Narayanan, A. Rebane, D. Lohse and E. Frey. We also thank V. Dhanvi and J. Govindan for manufacturing the acrylic molds.

## **Author contributions:**

S. G. and B. P. performed experiments, O. S. and A. G. designed and performed numerical simulations, A.G. designed research, analyzed data, and wrote the first draft of the manuscript. All the authors discussed the results and revised the manuscript.

## **Data and materials availability**

All data needed to evaluate the conclusions in the paper are present in the paper and/or the Supplementary Materials. Additional data related to this paper may be requested from the authors.

## **Supplementary materials**

### **Experimental methods**

#### **Chemical preparation**

The following chemicals and materials were used in this study. Sodium Bromate ( $\text{NaBrO}_3$ ), Sodium Bromide ( $\text{NaBr}$ ), Conc. Sulfuric acid (Conc.  $\text{H}_2\text{SO}_4$ ), Malonic acid [ $\text{CH}_2(\text{COOH})_2$ ], 1,4-Cyclohexane-dione, Ferrous sulfate, 1,10-phenanthroline was provided by sigma and used without any further purification. Ferroin was synthesized by mixing Ferrous sulfate hexahydrate and 1,10-phenanthroline in 1:3 molar ratio. For BZ-CHD experiments different concentration of the stock solutions were prepared in  $\text{dH}_2\text{O}$ . Solution A: (494.58 mM solution of Sodium bromate) Solution B: (891.9 mM solution of 1,4-cyclohexane-dione) Solution C: (971.9 mM solution of  $\text{NaBr}$ ). A mixture was prepared in a beaker by combining 9 mL of Solution A with 1.5 mL of Solution B, which was then homogenized using a magnetic stirrer. Following this, 1.5 mL of the Ferroin indicator was added to the mix. Under a chemical fume hood, 0.8 mL of Solution C was cautiously introduced to the reaction. The stirring continued for an

estimated 1 hour and 45 minutes. Subsequent to this phase, an additional 1.5 mL of Ferroin was incorporated into the mixture. The stirring persisted at a controlled temperature of 23°C for a further 30 minutes, after which it was halted. Attention was then given to the mixture for any signs of color transformation, signaling the start of wave propagation, typically observed 3.5 to 4 hours post the initial mixing process. Following the onset of color change, the BZ-CHD reaction mixture was transferred to a plasma-treated PDMS mold featuring an array of macro-pillars, as specified in Fig.S1A. These pillars, typically 1 mm in diameter and 3 mm high, are arrayed in a square grid with 5 mm spacing. In experiments with variable pillar dimensions and spacings, the volume of the BZ-CHD solution was adjusted to ensure a liquid height of about 1.5 mm, thus avoiding submergence of the pillars. Upon pouring, the solution was swirled gently until the mixture achieved a brown color. The Petri dish was then positioned undisturbed beneath a camera to record the wave propagation, under the illumination of white LED light. In some experiments, a smaller, modified 50 mm Petri dish was used, and the volume of the BZ-CHD solution was correspondingly reduced about 1.5 mL to maintain the same liquid height. It's important to note that in our standard setups, unless specified otherwise, the pillars do not submerge in the chemical solution. The hydrophilic nature of plasma-treated PDMS causes a thin layer of liquid to ascend the pillars (Fig.1B), altering the liquid surface near the obstacles as depicted in Fig. S1B.

For some experiments, the surface of the PDMS was coated with a 20 nm titanium layer and then with a pure gold layer. This was done using a Physical Vapor Deposition (PVD) technique with the Lesker Proline PVD 75 apparatus, rotating the substrate four times to achieve uniform coverage on the PDMS pillars' surfaces.

## Image Processing

The wave period is roughly one minute, and we capture images of the chemical waves at a rate of 1 frame per second across multiple wave cycles. To minimize spatial noise, we average the captured images over several wave cycles, typically 6-8, and then subtract each individual image from the time-averaged image. After this, we apply a Gaussian blur filter and use a customized Matlab code to perform the Hilbert transform, which helps us calculate the phase map. This code is provided in the Supplementary Information.

## Numerical methods

We used the three-component Tyson-Fife model [37] to simulate this system. The set of equations are:

$$\frac{du}{dt} = D \nabla^2 u + \frac{1}{\epsilon} (aw - uw + u - u^2) \quad (1)$$

$$\frac{dv}{dt} = u - v \quad (2)$$

$$\frac{dw}{dt} = \frac{1}{\epsilon'} (-aw - uw + bv) \quad (3)$$

where  $\epsilon' \ll \epsilon \ll 1$ ,  $a \ll 1$  and  $b \approx 1$ . The used parameters are as follows:  $D = 1$ ,  $\epsilon = 0.05$ ,  $\epsilon' = 0.001$ ,  $b = 2.5$  and  $a = 0.002$ . We note that at  $b = 2.5$ , the system is in the excitable state.

The model focuses on the essential dynamics of the reaction by reducing the full chemical mechanism to a manageable number of reactions and variables. It typically includes the rapidly varying activator  $u$  and the slowly changing inhibitors  $v$  and  $w$ , representing the concentrations of bromous acid ( $\text{HBrO}_2$ ), an oxidized form of the catalyst (such as ferroin  $\text{Fe}^{3+}$ ), and bromide ion ( $\text{Br}^-$ ), respectively.

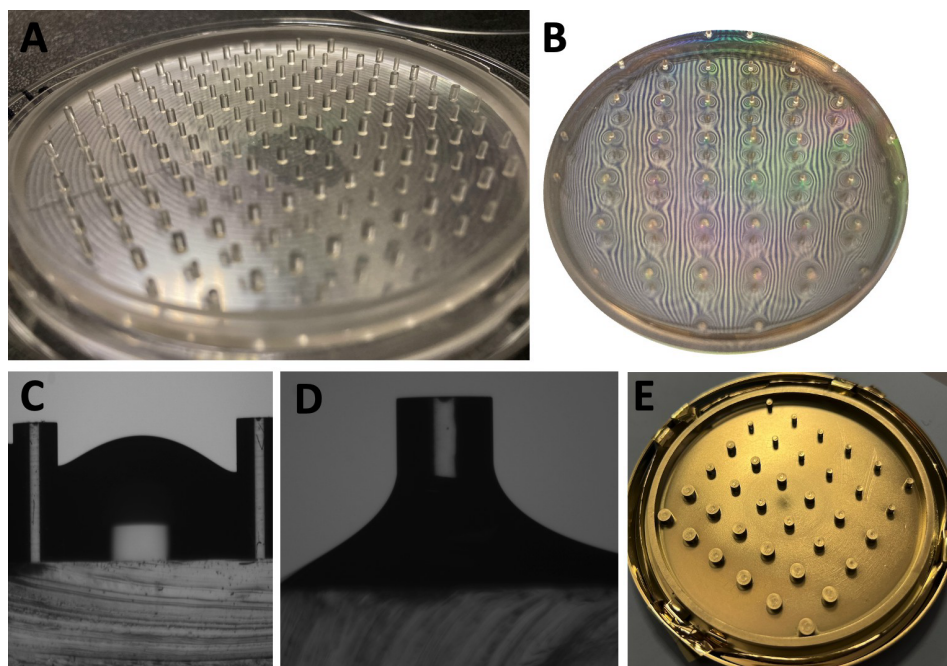


Figure S1: **Experimental design.**(A) A PDMS mold featuring alternating pillar diameters of 1 mm and 1.5 mm was utilized in the experiment shown in Fig. 2. The PDMS mold includes both pillars and PDMS walls around the edges, tailored to fit a standard 100 mm Petri dish. (B) A striped pattern is projected onto the fluid surface to illustrate the deformation caused by the hydrophilic pillars. (C-D) The profile of the fluid near the pillars is analyzed before and after plasma treatment. (E) A sample of a PDMS mold that has been coated with a thin layer of gold.

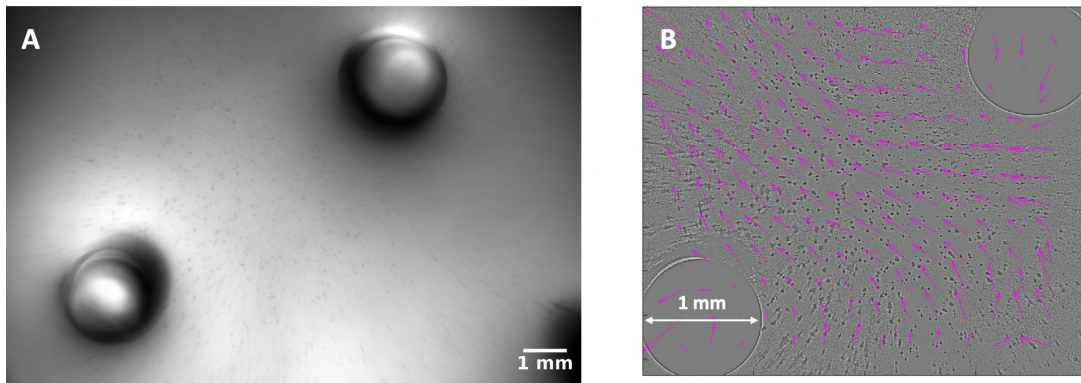


Figure S2: **Marangoni-driven surface flows.** A-B) In this experiment, tracer particles ( $20\ \mu\text{m}$  in diameter) are utilized to visualize surface flows driven by Marangoni effects, primarily caused by gradients in chemical concentration that create surface tension gradients (refer to Video 12).

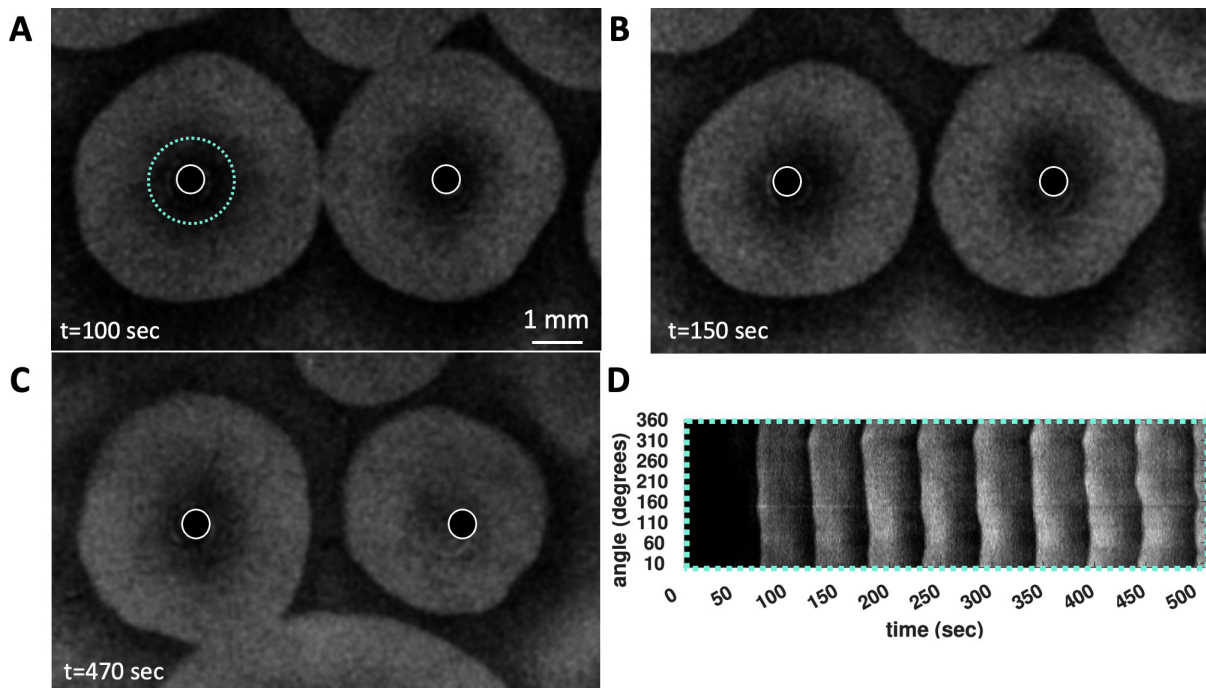


Figure S3: **No fingering instability in small diameter pillars.** In experiments conducted with open-lid Petri dishes featuring pillars of 0.5 mm diameter, there is no occurrence of wave front instability. This observation indicates that a certain minimum perimeter of the pillars is necessary for fingering instability to occur. Additionally, the space-time plot shown in panel **D** is created by accumulating the light intensity around the cyan-colored circle depicted in panel **A**.

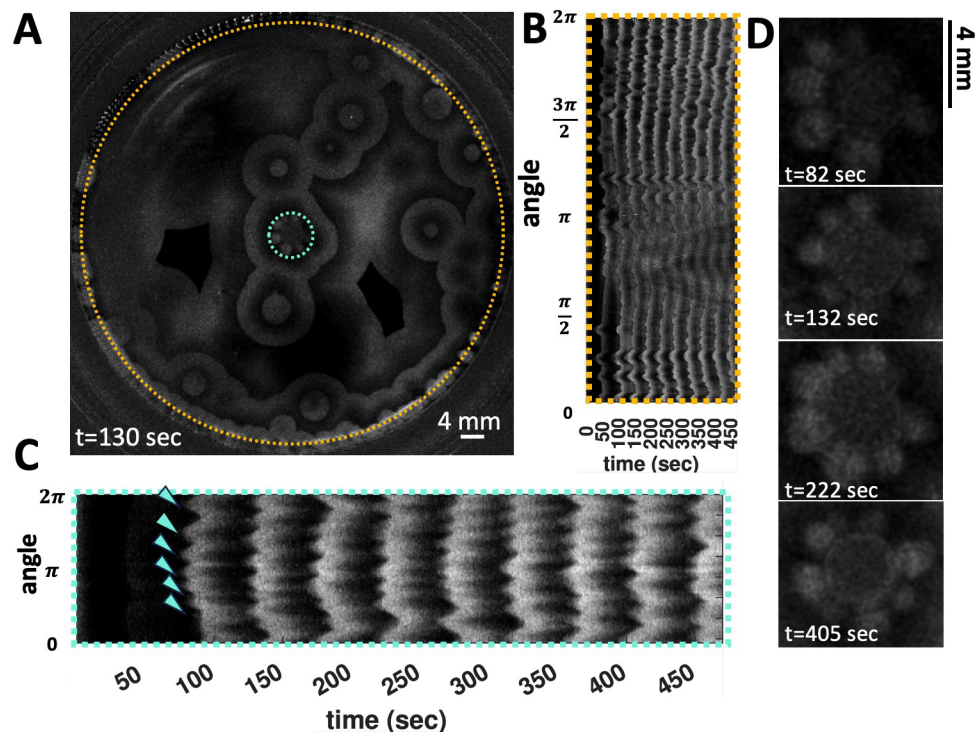


Figure S4: **A single pillar also acts as the wave center.** (A-C) An isolated pillar serves as the wave center and exhibits wavefront instability in an open setup. Additionally, we observe wavefront instability at the PDMS walls around the periphery. (D) shows a flower-like pattern with six or seven petals at different time points that formed around the solitary central pillar.

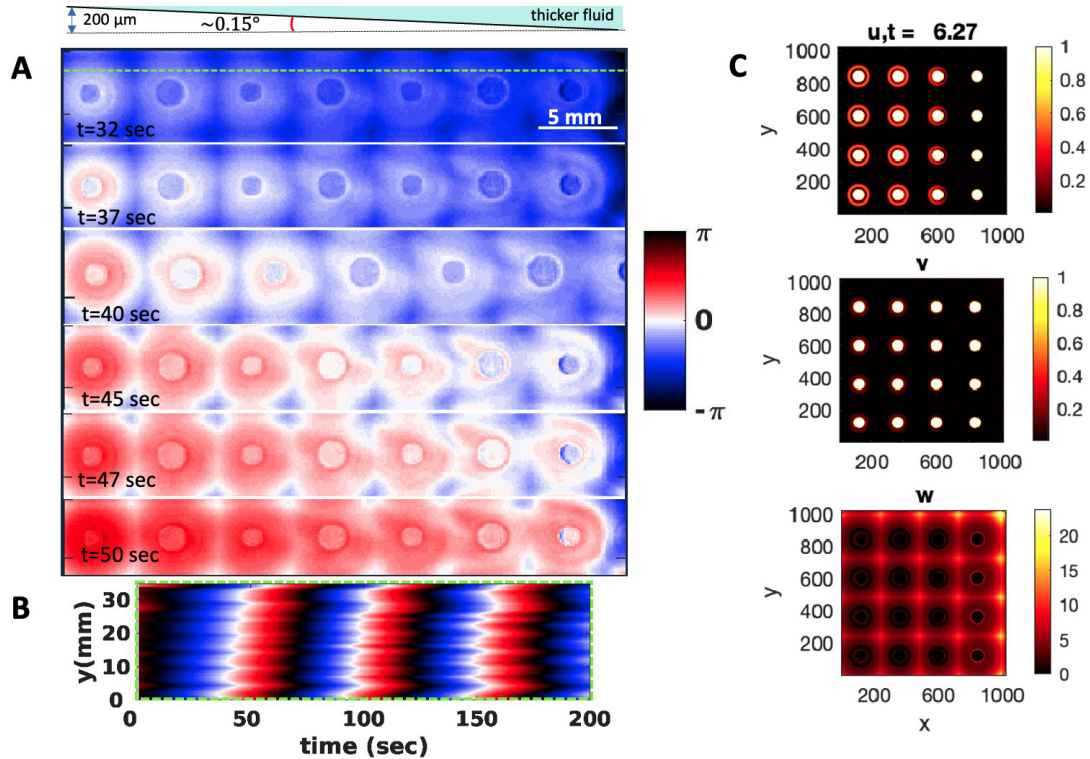


Figure S5: **Propagation of phase waves in a slightly tilted Petri dish.** (A) In a Petri dish with a slight tilt, synchronization waves initiate in the thinner part of the fluid and propagate towards the area with greater fluid thickness. (B) Space-time plot of the phase map along the green dashed line indicated in panel A illustrates the propagation of phase waves. Notice that in this experiment, the lid is open, and flower patterns emerge at  $t \sim 80\ \text{sec}$  (see Video 13). (C) Numerical simulations emulating the experimental setup. Details on the simulations can be found in the SI.

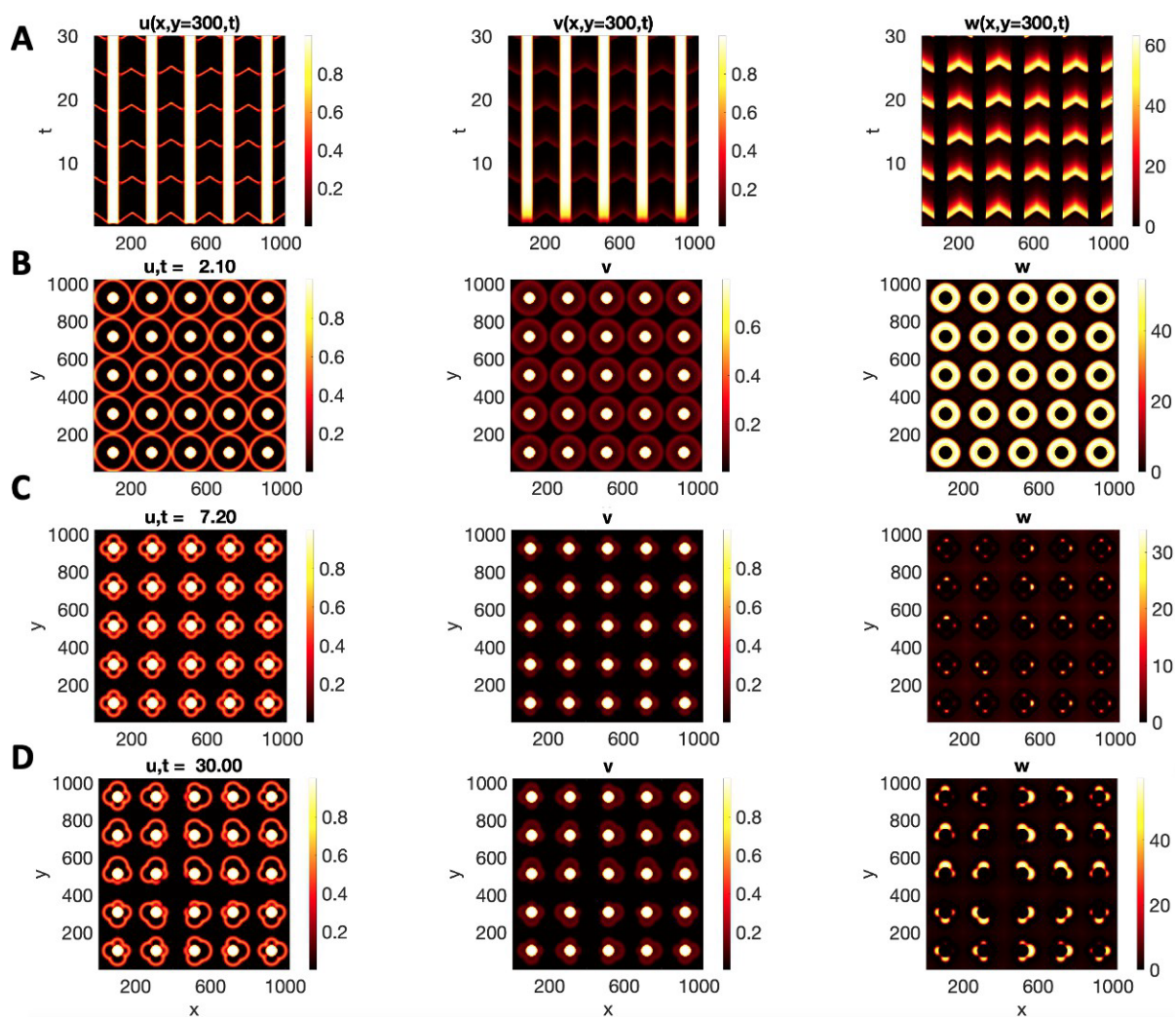


Figure S6: Numerical simulations with asymmetric  $w$  around the pillars as defined in the SI. (A) The space-time plot along the line marked in panel B illustrates that the obstacles become wave centers. (B) shows an image of the circular waves emanating from the obstacles. (C-D) Over time, the wavefront breaks, leading to the emergence of flower-like wave patterns.

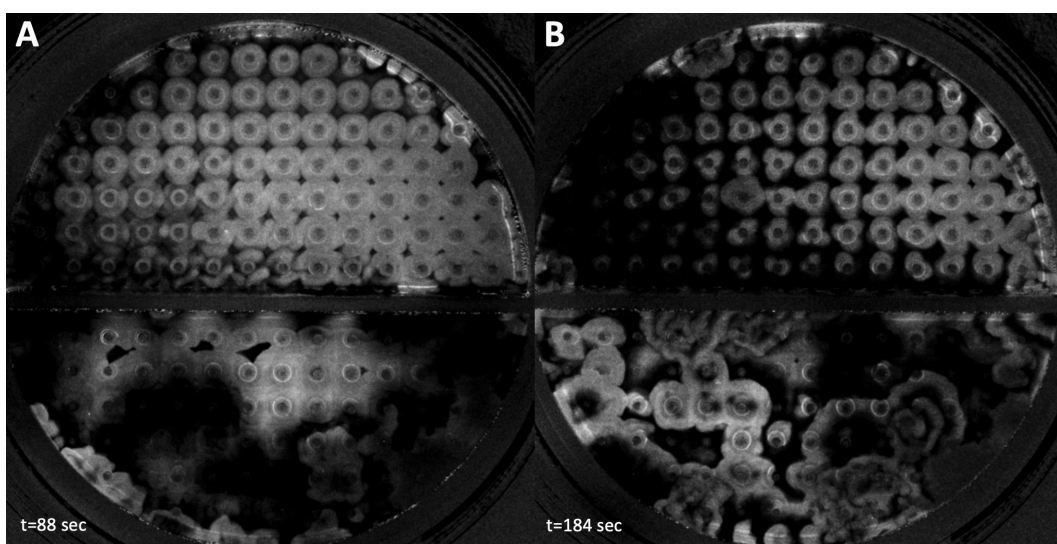


Figure S7: **Hydrophilic versus hydrophobic obstacles:** An overview of a partitioned, open-lid Petri dish taken at two distinct times: before (**A**) and after (**B**) the emergence of instability. The upper portion of the dish has been plasma-treated to render PDMS hydrophilic, whereas the lower section has been left untreated, maintaining its hydrophobic properties.

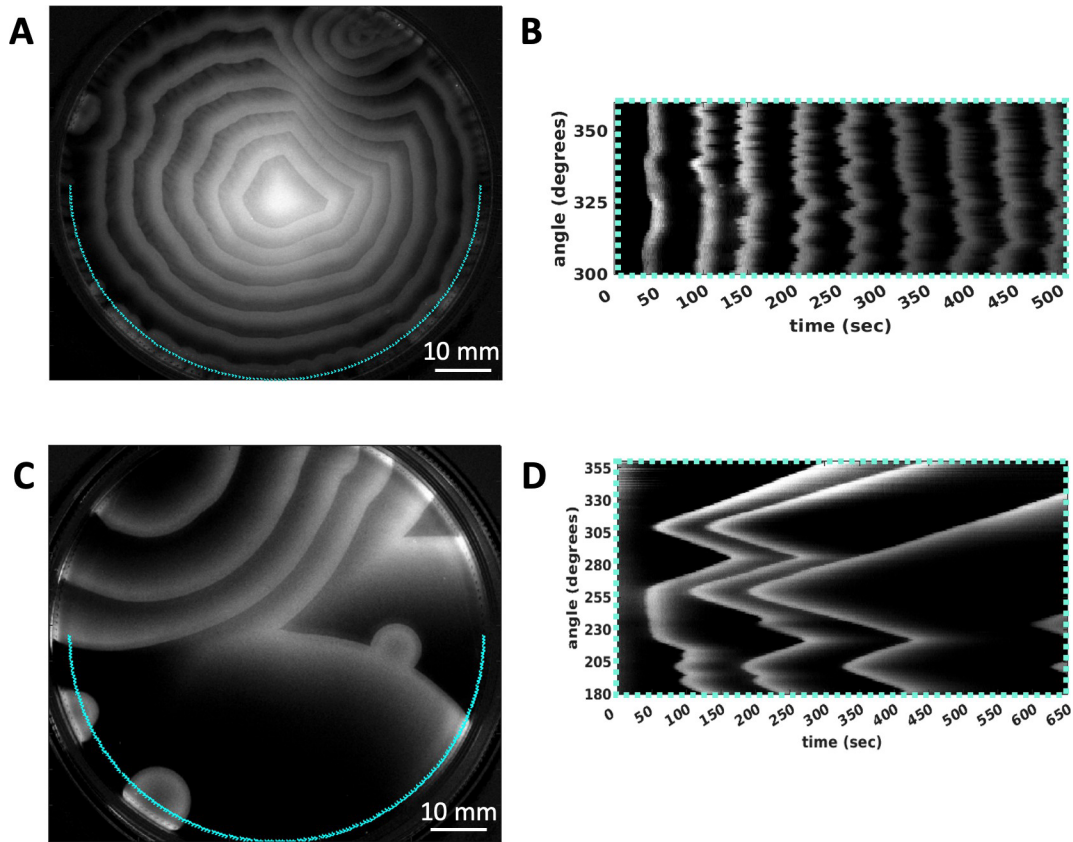


Figure S8: **Experiment in a glass Petri dish without obstacles.** (A) A top view of a glass Petri dish with an open lid and plasma treatment, illustrating fingering instability at the glass boundary. Notice that rippled waves travel and make visible the underlying mosaic patterns generated by the Marangoni instabilities. (B) A space-time plot along the cyan-colored semi-circle shows the dynamics of the fingering, emphasizing that the positions of the fingers can change over time. (C-D) A setup similar to panel A, but with a closed lid. In this configuration, wave centers appear at the periphery, but the wave fronts maintain their circular forms.